Analysis of the Fragmentation of AlON and Spinel Under Ballistic Impact

Elmar Strassburger[1]

e-mail: elmar.strassburger@emi.fraunhofer.de

Martin Hunzinger

Fraunhofer Institute for High-Speed Dynamics,
Ernst-Mach-Institute (EMI),
Am Christianswuhr 2,
79400 Kandern, Germany

Parimal Patel

James W. McCauley

U.S. Army Research Laboratory,
AMSRD-ARL-WM-MD,
Aberdeen Proving Ground, MD 21005

It has been demonstrated that significant weight reductions can be achieved, compared to conventional glass-based armor, when a transparent ceramic is used as the strike face on a glass-polymer laminate. Magnesium aluminate spinel ($MgAl_2O_4$) and AlON are promising candidate materials for application as a hard front layer in transparent armor. Comprehensive, systematic investigations of the fragmentation of ceramics have shown that the mode of fragmentation is one of the key parameters influencing the ballistic resistance of ceramics. In the study described here, the fragmentation of AlON and three types of spinel was analyzed: two types of fine grained spinel with nominal average grain sizes 0.6 μm and 1.6 μm and a bimodal grain-sized spinel with large grains of 250 μm size in a fine grain (5–20 μm) matrix were examined. The ceramic specimens of 6-mm thickness were glued to an aluminum backing and impacted with armor piercing (AP) projectiles of caliber 7.62 mm at two different velocities—850 m/s and 1100 m/s. The targets were integrated into a target box, which allowed for an almost complete recovery and analysis of the ceramic fragments. Different types of high-speed cameras were applied in order to visualize the different phases of fragment formation and ejection. A laser light-sheet illumination technique was applied in combination with high-speed cameras in order to determine size and speed of ejected ceramic fragments during projectile penetration. The application of the visualization techniques allowed for the analysis of the dynamics of the fragment formation and interaction with the projectile. A significant difference in the fragment size distributions of bimodal grain-sized spinel and AlON was observed.
[DOI: 10.1115/1.4023573]

1 Introduction

Transparent armor is one of the most critical components in the protection of light-armored vehicles. Typical transparent armor consists of several layers of glass with polymer interlayers and backing. The design of transparent laminates for ballistic protection is still mainly an empirical process. Considering the high number of parameters influencing the performance, like number, thickness and type of the glass layers, thickness and type of the bonding layers, and the polymer backing, the necessity to have tools for a systematic optimization becomes obvious. The number of parameters is even extended with an additional front layer of a transparent ceramic, which has been proven to enhance the efficiency of transparent laminates against armor-piercing ammunition significantly [1–3]. Due to the high number of influencing parameters, a detailed understanding of the dominant mechanisms during projectile penetration is required in order to improve the performance of multilayer, ceramic-faced transparent armor. On one hand, a high ballistic resistance is related to projectile deformation and erosion. On the other hand, the resistance to penetration, and therefore the ability to deform and erode the projectile, depends on the damage and failure mechanisms in the target materials. Since part of transparent armor consists of brittle materials, the fragmentation of the ceramic and glass layers plays a key role in the resistance to penetration [4,5].

Curran et al. [6] investigated the dynamic fragmentation of brittle materials and developed models in order to predict fragment sizes. They described the fracture process in three stages: crack nucleation, crack growth, and crack coalescence. This description is based on the assumption of an inherent distribution of flaws, which are the sites of fracture nucleation, depending on the loading. Shockey et al. [5] recently investigated the failure of glass due to the penetration of steel projectiles of size and shape similar to the steel cores of armor-piercing ammunition. The data derived from the postpenetration analysis of the fragmentation were used as a basis for modeling material failure and projectile penetration [7]. In these models, the resistance to penetration into ceramic and glass is mainly attributed to residual strength, determined by friction and flow characteristics of the failed material.

In a comprehensive study on the parameters influencing the ballistic resistance of ceramics, the hypothesis of a hierarchic order of the influences has been confirmed [8,9]. The results indicate that the mode of fragmentation, i.e., the distribution of the fragment sizes, is playing a critical role with respect to the erosion of the projectile by the ceramic fragments.

In order to analyze the fragmentation of the different types of ceramics, a target setup was designed that allowed for an almost complete recovery and analysis of the ceramic fragments. Since an analysis of the recovered ceramic debris after the completed ballistic test cannot reveal which of the fragments interacted at what time with the penetrator, different visualization techniques were applied in order to observe the fragmentation and the ejected ceramic particles during projectile penetration.

2 Experimental Configuration and Techniques

An armor-piercing (AP) projectile of caliber 7.62 mm × 51 with steel core and a total mass of 9.5 g was chosen for the test series.

Report Documentation Page		Form Approved OMB No. 0704-0188

1. REPORT DATE **MAY 2013**	2. REPORT TYPE	3. DATES COVERED **00-00-2013 to 00-00-2013**
4. TITLE AND SUBTITLE **Analysis of the Fragmentation of AlON and Spinel Under Ballistic Impact**		5a. CONTRACT NUMBER
		5b. GRANT NUMBER
		5c. PROGRAM ELEMENT NUMBER
6. AUTHOR(S)		5d. PROJECT NUMBER
		5e. TASK NUMBER
		5f. WORK UNIT NUMBER
7. PERFORMING ORGANIZATION NAME(S) AND ADDRESS(ES) **U.S. Army Research Laboratory,AMSRD-ARL-WM-MD,Aberdeen Proving Ground,MD,21005**		8. PERFORMING ORGANIZATION REPORT NUMBER
9. SPONSORING/MONITORING AGENCY NAME(S) AND ADDRESS(ES)		10. SPONSOR/MONITOR'S ACRONYM(S)
		11. SPONSOR/MONITOR'S REPORT NUMBER(S)
12. DISTRIBUTION/AVAILABILITY STATEMENT **Approved for public release; distribution unlimited**		
13. SUPPLEMENTARY NOTES **Journal of Applied Mechanics, MAY 2013, Vol. 80**		
14. ABSTRACT		
15. SUBJECT TERMS		

16. SECURITY CLASSIFICATION OF:			17. LIMITATION OF ABSTRACT	18. NUMBER OF PAGES	19a. NAME OF RESPONSIBLE PERSON
a. REPORT **unclassified**	b. ABSTRACT **unclassified**	c. THIS PAGE **unclassified**	**Same as Report (SAR)**	**11**	

Standard Form 298 (Rev. 8-98)
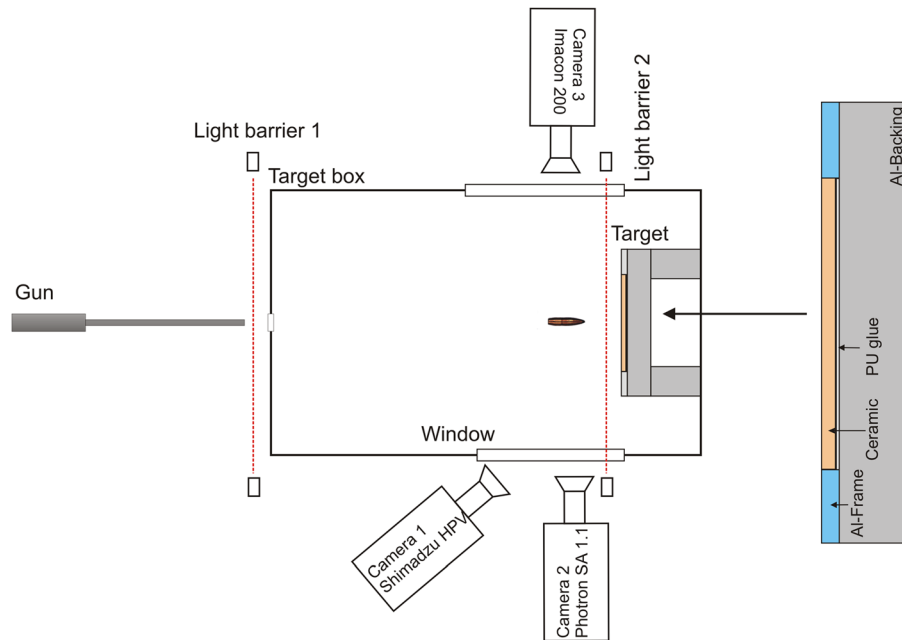Prescribed by ANSI Std Z39-18

Fig. 1 Schematic of ballistic test configuration (left) and target (right)

The steel cores had a mass of 3.7 g and a length of 23.5 mm. The tests were conducted at two different impact velocities, nominally, 850 m/s and 1100 m/s. The complete interaction of the projectile with the target should comprise three phases: dwell, ceramic penetration, and backing penetration. Since the threshold ceramic thickness for the case of no penetration of the 7.62-mm AP projectile is very low with ceramic-steel targets, aluminum was chosen as the backing material. The plates of Al 2017 A with a tensile strength 400 MPa had the dimensions $200 \times 200 \times 25$ mm. The dimensions of the fine-grained spinel specimens were approximately $90 \times 90 \times 5.7$ mm, whereas, the bimodal grain-sized spinel and the AlON specimens were $100 \times 100 \times 6$ mm. The ceramic tiles were bonded to the aluminum backing with polyurethane glue. The thickness of the bonding layer was 0.8 mm for all targets. The ceramic tiles were laterally surrounded by an aluminum frame with a small air gap of a few tenths of a millimeter between the ceramic and the frame. The aluminum frame was utilized to keep the ceramic fragments outside the interaction zone in place and not as a confinement. The target was integrated in a target box, which allowed for an almost complete recovery and analysis of the ceramic fragments. The ceramic fragments were extracted from the target chamber through a chain of sieves and separated into size classes. Figure 1 shows a schematic of the ballistic test configuration and the target.

Different methods were applied to observe and analyze the fragmentation of the impacted ceramics. The first method was the recovery and size analysis of the ceramic fragments after the ballistic tests were completed. The conglomerate of projectile and ceramic fragments was extracted from the target box and collected in a sieve fabric of 25-μm mesh size. Bigger parts of the projectile jacket were sorted out manually; all ferrous particles were separated from the ceramic by means of a magnet. The ceramic fragments were separated into size classes by a chain of sieves. The mesh sizes used were 2 mm, 1 mm, 0.5 mm, 200 μm, 100 μm, 63 μm, and 25 μm. The total mass of each size fraction was determined. The dimensions and weight of the spinel specimens as well as the weight of the complete targets before and after the impact test were measured in order to determine the fraction of recovered ceramic particles.

Three types of high-speed cameras were applied in order to visualize different phases of the fragment formation and ejection. A high-speed video camera was utilized to observe the formation,

development, and structure of the fragment cloud over a time period of several milliseconds. The beginning of the projectile target interaction with the flow of projectile material at the surface of the ceramic, crack propagation in the ceramic, and the onset of the ejection of fragments were visualized with an ultra-high-speed video camera, which allows recording a total number of 100 frames at a maximum rate of 10^6 frames per second. An Imacon 200 high-speed camera was utilized to measure the maximum velocity of the ejected fragments.

3 Ballistic Results

Aluminum oxynitride (AlON — $Al_{23}O_{27}N_5$, Surmet, Burlington, MA) and three different types of $MgAl_2O_4$ spinel were examined. The two types of fine-grained spinel with nominal average grain sizes of 0.6 μm and 1.6 μm were manufactured by A. Krell at the Fraunhofer IKTS, Dresden, Germany. The bimodal grain-sized spinel with large grains of about 250 μm in a fine grain (5–20 μm) matrix was manufactured by TA&T, Annapolis, MD. Since AlON also has the spinel crystal structure, in essence, four spinel materials with different microstructure were examined. Table 1 lists some of the physical and mechanical properties; Fig. 2 illustrates the various microstructures. Six specimens of each material were tested. With each material, three tests were conducted at 850-m/s impact velocity and three at 1100 m/s, respectively. The test matrix and ballistic results are shown in Table 2.

Table 1 Material properties

Material	Average grain size (μm)	Density (g/cm^3)	Elastic modulus (GPa)	Weibull modulus	Fracture toughness K_{IC} (MPa$\sqrt{m}$)
Spinel 205[a]	0.6	3.58	277[b]	19.5[b]	1.72[b]
Spinel 200[a]	1.6				
Bimodal spinel[c]	5–20/100–200				
AlON[d]	150–200	3.67	315[b]	8.7[b]	2.4[b]

[a]A. Krell, Fraunhofer IKTS, Dresden, Germany.
[b]Typical data [2].
[c]TA&T, Annapolis, MD.
[d]Surmet, Burlington, MA.

Spinel 205: 0.6 μm   (a)

Spinel 200: 1.6 μm   (b)

AlON: 150-200 μm   (c)

Bimodal spinel: fine grain size: ~ 5-20 μm
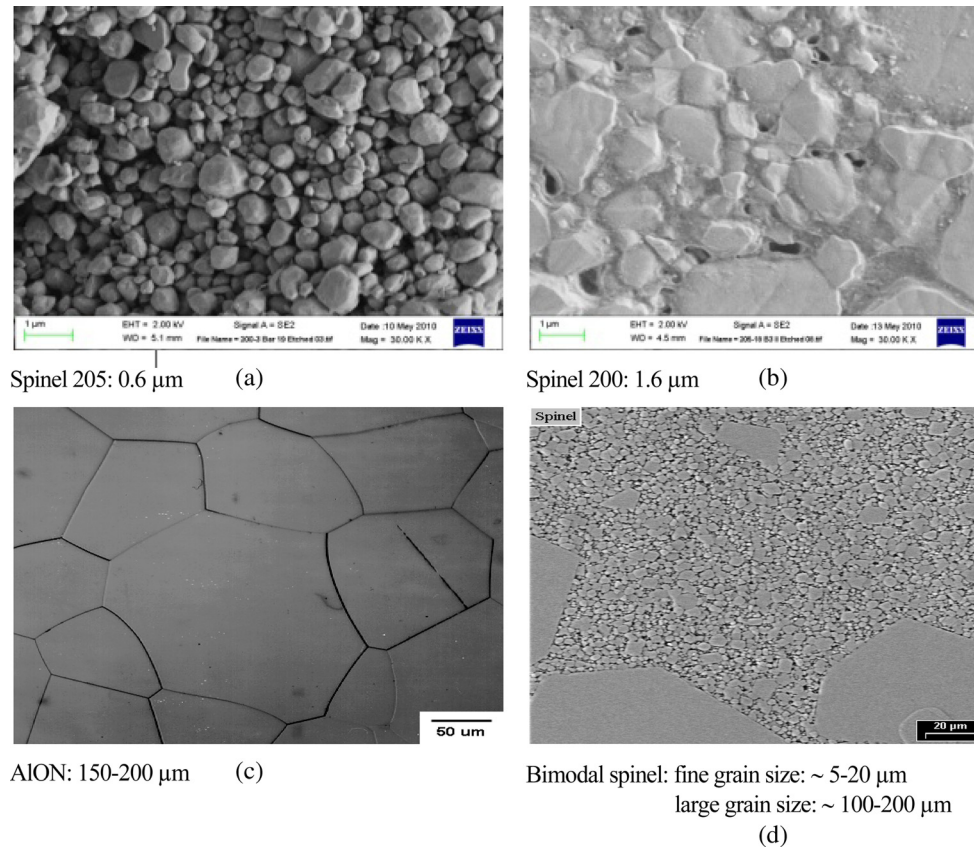large grain size: ~ 100-200 μm
(d)

Fig. 2 Microstructure of the tested materials

Table 2 Ballistic results

Material	Impact velocity (m/s)	Mean residual penetration (mm)	Mean residual core mass (mm)
Spinel 205	850	1.2	1.37
	1100	16.3	2.17
Spinel 200	850	1.1	1.55
	1100	15.8	1.95
Bimodal spinel	850	1.8	1.72
	1100	15.9	2.2
AlON	850	0.5	1.04
	1100	9.2	2.02

(a)

(b)

Fig. 3 Photographs of residual projectile material from tests with AlON at 850 m/s (top) and 1100 m/s (bottom)

The three types of spinel exhibited almost the same ballistic resistance. At 850-m/s impact velocity, nearly no penetration into the backing aluminum plate was observed with all materials. At 1100 m/s, a clear difference between the spinel types and AlON could be recognized. The mean residual penetration was $P_R = 9.2$ mm with AlON, whereas a P_R of about 16 mm was observed with all spinels.

In all tests, strong erosion of the steel core was observed. The eroded material that was recovered from the target box mainly consisted of very small particles. A significant difference was observed at the two different impact velocities. Projectile erosion and fragmentation was much stronger at 850 m/s with all materials. Only small pieces that could be determined to be from the rear part of the steel core were found. The residual core masses given in Table 2 for shots at 850 m/s are the sum of the masses of one to four bigger pieces. The strongest erosion was observed with AlON at 850 m/s. The average mass of the residual part of

the steel core was 1.04 g. At 1100-m/s impact velocity, one big residual part of the steel core was found in each test. Figure 3 illustrates the difference in projectile erosion and fragmentation at the different impact velocities.

4 High-Speed Photography and Crack Velocity Measurement

Tests were conducted with each material at both impact velocities, which were fully instrumented for high-speed photography. Three types of cameras were utilized in order to visualize different aspects of the projectile-target interaction and the fragment formation and ejection. The beginning of the projectile target interaction, crack propagation, and the onset of the ejection of fragments were visualized with an ultra-high-speed Shimadzu HPV video camera, which allows for recording a total number of 102 frames at a maximum rate of 10^6 frames per second.

Selections of five high-speed photographs of the projectile impact at 1100 m/s on 0.6- and 1.6-μm spinels, AlON, and bimodal grain-sized spinel, respectively, are presented in Fig. 4. The frame rate was 1 MHz. These high-speed photographs show that radial cracking starts immediately with the impact of the projectile. Ring-shaped zones of damaged material can also be recognized, surrounding the radial crack zone during the first microseconds. The radial cracks cross the ring cracks after about 3–4 microseconds. The radial cracks propagate at a higher velocity compared to the expansion of the circular damage zone in the center.

For all materials tested, the positions of crack tips were measured, and the propagation velocity was determined by linear regression of the data. Figure 5 shows examples of path-time histories of crack propagation for the 0.6-μm spinel, bimodal spinel, and AlON impacted at 850 m/s. This figure also illustrates the radial cracks selected for velocity measurements. Since all radial cracks originate from the point of impact and start propagating at about the same time, offsets on the time axis of 0.5–2 μs were added to the time coordinates of cracks B, C, and D in the diagrams of Fig. 5 for the sake of clarity in the presentation of the
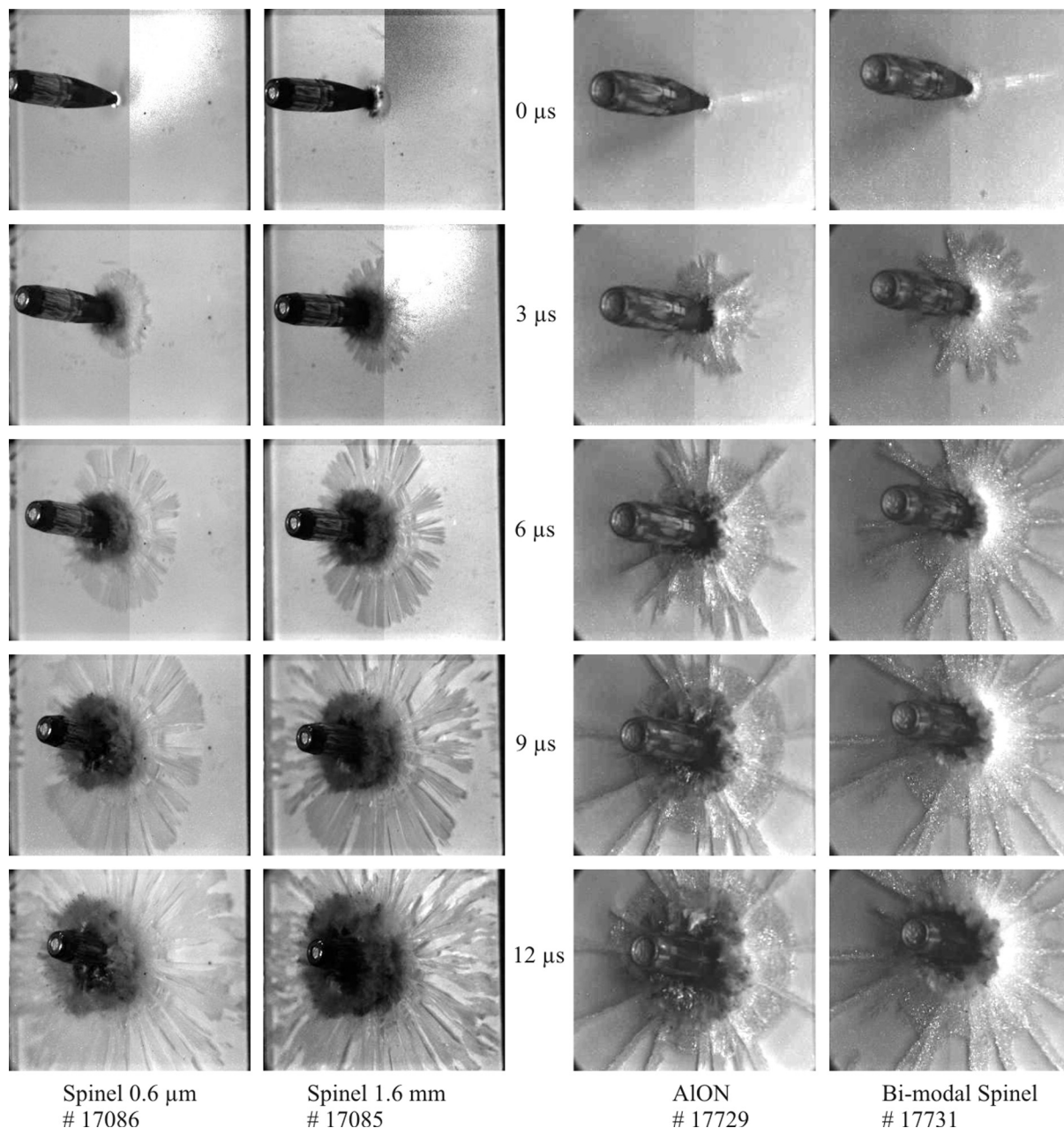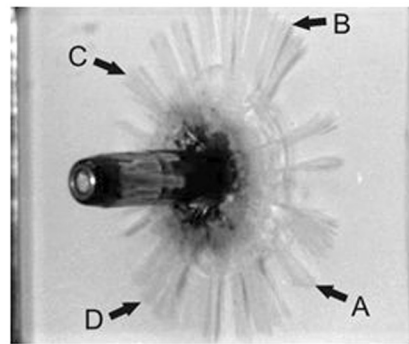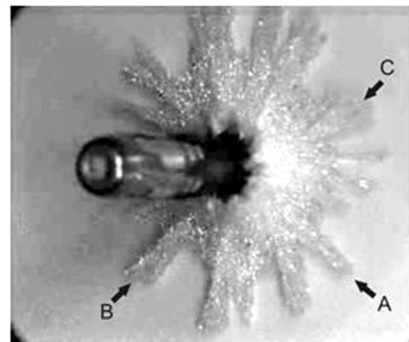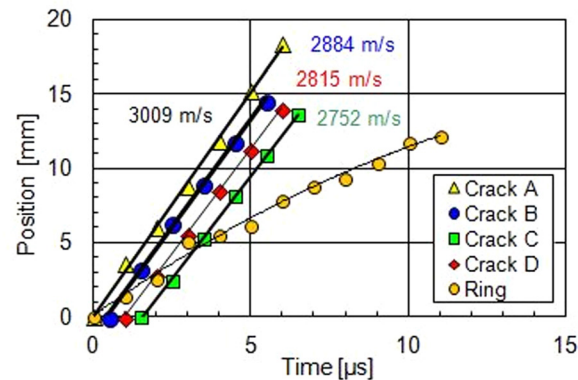

Fig. 4 Selection of five high-speed photographs of AP projectile impact on four spinels at 1100 m/s
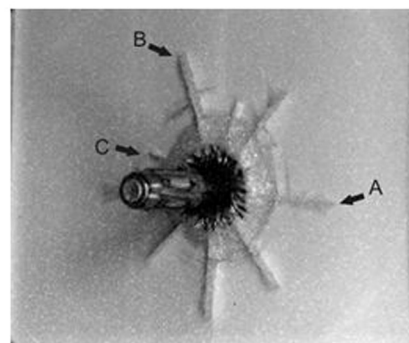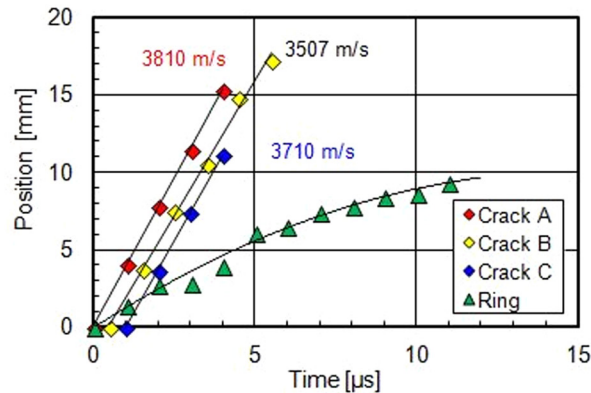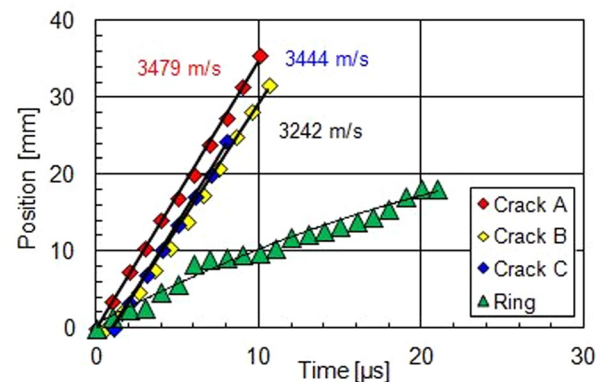
Fig. 5 High-speed photographs illustrating crack nomenclature (left) and path-time histories of radial crack propagation and circular damage zone expansion (right) for spinel 205, bimodal spinel, and AlON impacted at 850 m/s

data. The expansion velocity of the circular damage zone was also determined from the high-speed photographs. The data indicate a decrease of the expansion velocity with time, and therefore, a second order polynomial fit was chosen for approximation of the data. The expansion velocity was then determined from the slope of the curves at different times. Table 3 summarizes the complete set of crack velocities and circular damage zone expansion velocities determined at the two impact velocities with the four materials. The number and exposed surface morphology of the radial cracks in the four spinel structure materials are markedly different, clearly demonstrating an apparent microstructural effect. This is particularly interesting, since all four materials, including AlON, have spinel crystal structures and comparable intrinsic properties. Preliminary observations of the radial cracks indicate that the fine-grain spinels exhibit a higher density/number of radial cracks and much more crack bifurcation and branching than the bimodal and AlON materials. With the bimodal grain-sized

spinel, light was reflected from a high number of small spots along the cracks, which gave them a sparkling appearance suggestive of a more rough surface morphology. The reflections were caused presumably by newly generated fracture surfaces along the boundaries of the very large grains. Averaging the radial crack velocities at the 850- and 1100-m/s impact velocities results in the following: 0.6-μm spinel $\approx$ 2929 m/s; 1.6-μm spinel $\approx$ 3056 m/s; AlON $\approx$ 3566 m/s; and bimodal spinel $\approx$ 3722 m/s. The magnitude and rate of energy dispersion and dissipation of crack propagation via intragranular/intergranular mechanisms in the four microstructures will clearly impact the radial crack velocities, and this will be followed up in future work.

The mean expansion velocities of the circular damage zone in the center were up to 1650 m/s during the first microseconds but then decreased to about 500 m/s over a period of about 10 μs in some cases. Due to different camera set-ups and image sections selected during the experimental program, the expansion of the

Table 3 Crack velocities

Material	Impact velocity (m/s)	Test #	Radial crack velocities (m/s)	Mean velocity radial cracks (m/s)	Std. dev. (m/s)	Expansion vel. circular zone (m/s)	
						2 μs	10 μs
Spinel 205	850	17,087	3009, 2884, 2815, 2752	2865	110	1346	780
	1100	17,086	2827, 3057, 3099, 2985	2992	120	1423	1197
Spinel 200	850	17,084	2954	2954	—	1251	426
	1100	17,085	2988, 3299, 3299, 3045	3158	165	1018	507
Bimodal spinel	850	17,730	3810, 3507, 3710	3701	144	1160	450
		17,733	3539, 3817, 3823			1124	820
	1100	17,731	3827, 3768, 3929	3742	135	1445	453
		17,732	3749, 3554, 3626			—[a]	—[a]
AlON	850	17,724	3626, 3743	3507	190	1500	500
		17,726	3479, 3242, 3444			1080	863
	1100	17,728	3829, 3732	3624	296	—[a]	—[a]
		17,729	3817, 3114, 3628			1645	470

[a]Measurement not possible.

Table 4 Mean terminal crack velocities $\overline{v_{cr}}$ and Rayleigh wave speeds c_R

|	Shear modulus G (GPa)	Transvers. wave speed $c_T = \sqrt{G/\rho}$ (m/s)	Poisson's ratio ν	Rayleigh wave speed c_R[a] (m/s)	$\overline{v_{cr}}/c_R$
Spinel	192 [18]	7323	0.26	6737	0.43 (fine-grained) 0.55 (bimodal)
AlON	135 [19]	6040	0.24	5557	0.65

[a]$c_R \cong 0.92\, c_T$ for Poisson's ratio $\nu = 0.25$ [10].

circular damage zone could not be observed over the same time interval in all tests.

The radial cracks are generated by tensile stresses, since the material in the vicinity of the point of impact is displaced by a compression wave. Due to the compressive stresses, the diameter of a circular zone around the center of impact is increasing, which causes high tangential tensile stresses that initiate fracture in a perpendicular, i.e., radial direction [10]. The radial crack velocity measurements have demonstrated fairly constant crack speeds during the time interval of observation. Several researchers have investigated the issue of terminal crack velocities in brittle materials. A comprehensive summary of the different approaches has been given recently by Yavari and Khezrzadeh [11]. Several theoretical treatments of the problem of stable crack propagation have predicted a terminal crack velocity of about 50% of the Rayleigh wave velocity c_R [12–14], depending on Poisson's ratio of the material. These results have been confirmed experimentally for brittle amorphous materials, like PMMA [15] and different types of glass [16]. Ravi-Chandar and Knauss [17] concluded from their studies that the terminal crack velocity is not a fixed fraction of the Rayleigh wave speed and that this fraction is material-dependent. Yavari and Khezrzadeh [11] also predict a material-dependent terminal crack velocity in the range (0.5–0.557 c_R) and (0.539–0.557 c_R) for plane stress and plane strain, respectively.

The terminal crack velocities observed with the three types of spinel and AlON are compared to the Rayleigh wave speeds in Table 4. With the fine-grained spinels, the terminal crack velocities were about 44% of c_R. For the bimodal spinel [18], a terminal crack velocity of 55% and with AlON [19] of 66% of c_R were observed.

The formation of the circularly shaped damage zone in the center is caused by the reflection of the spherical stress wave at the rear side of the ceramic plates. Due to the high velocity of the longitudinal wave and the limited ceramic thickness (6 mm), the wave is reflected after less than one microsecond as a tensile wave, expanding radially and causing damage to the brittle material. Due to the decreasing amplitude of the radially expanding
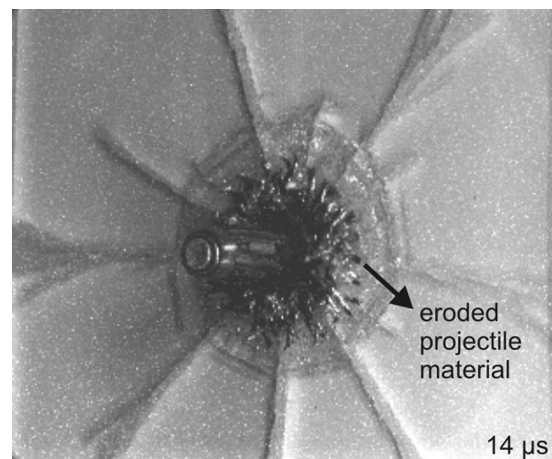
Fig. 6 High-speed photograph from impact on AlON at 850 m/s, test no. 17,726

stress wave and the interaction with predamaged material, the expansion velocity of the damaged zone decreases rapidly.

From the high-speed photograph of the projectile-target interaction in Fig. 6, it can be recognized that projectile material (black) is flowing radially outward at the surface of the AlON ceramic, indicating a phase of dwell and erosion before penetration. Projectile erosion before penetration could not be clearly observed with the other types of spinel tested. This finding corresponds to the lower residual penetration and lower residual masses of the steel cores determined in the tests with AlON (Table 2). However, projectile erosion cannot only be attributed to a dwell phase, since considerable erosion of the steel cores was also observed with the other three spinels. The results indicate that, in those cases, the erosion mainly occurred during penetration of the ceramic. This phase of interaction can only be visualized by means of flash
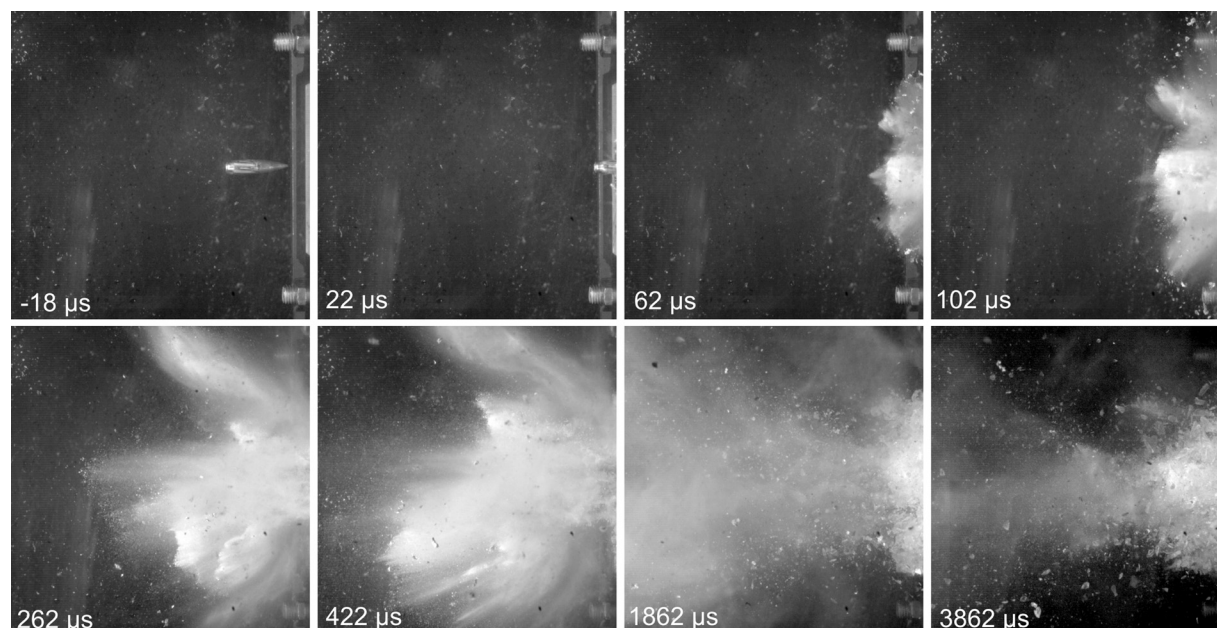
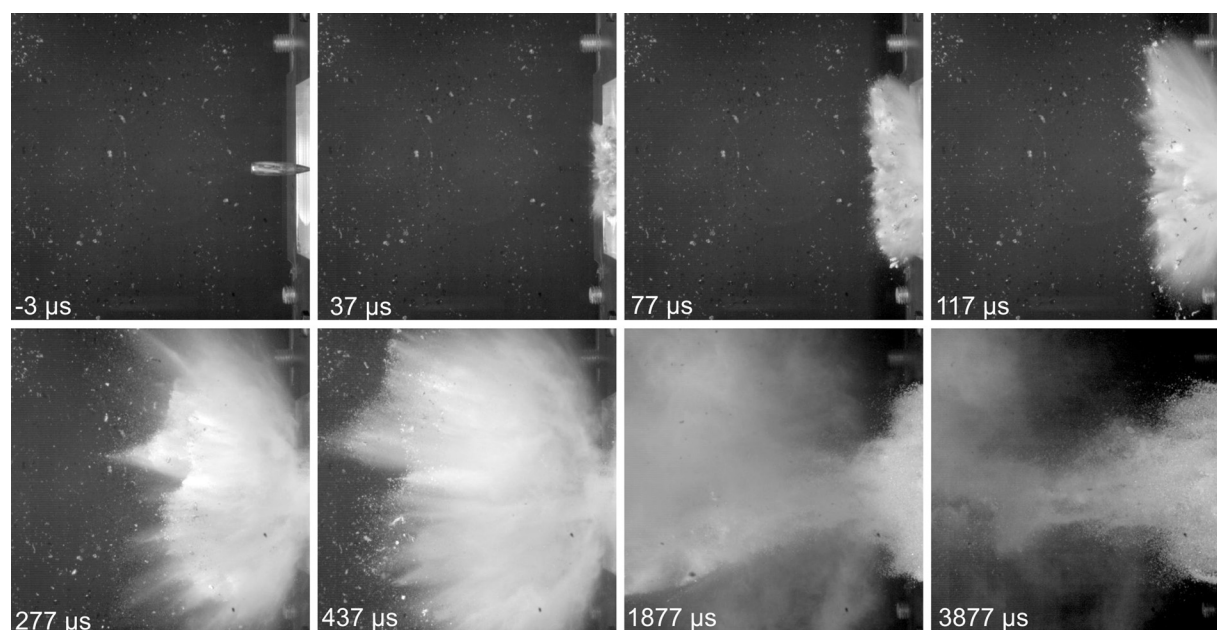**Fig. 7   High-speed photographs of fragment ejection from AlON, impact velocity 850 m/s**

Fig. 8   High-speed photographs of fragment ejection from bimodal spinel, impact velocity 850 m/s

X-ray techniques. Investigations to determine the contributions of the different phases (dwell and penetration) to projectile erosion will be the subject of future work.

The ejection of ceramic fragments from the crater and the fragmented area of the ceramic specimen are illustrated in Figs. 7 and 8 for AlON and the bimodal spinel at 850-m/s impact velocity, respectively. With AlON, the ejection of particles started at about 30 μs after impact. This delay is in agreement with the findings from the high-speed photographs presented in Fig. 6, where a strong flow of projectile material at the surface of the AlON specimen occurred, whereas immediate projectile penetration into spinel was observed. The average velocity of the ceramic particle front was 545 m/s with AlON and 386 m/s with the bimodal spinel. However, velocities of up to 600 m/s were measured for bigger, single-spinel particles that passed by the front of the fine debris.

5   Fragmentation Analysis

5.1   Results of Sieve Analysis. The ceramic fragments were separated into size classes by a chain of sieves. The mesh sizes used were 2 mm, 1 mm, 0.5 mm, 200 μm, 100 μm, 63 μm, and 25 μm. The total mass of each size fraction was determined. Three tests were conducted with each material at two impact velocities. Figure 9 presents the mean values of the total fragment mass in the different size classes for all configurations. Figure 10 shows the fragment mass data of the single tests with AlON at both impact velocities in order to illustrate the relatively small spread in the data. With AlON and the fine-grained spinel types, a decrease of the total fragment mass was observed with decreasing mesh size. In contrast to these materials, the bimodal grain-sized spinel exhibited a very clear maximum in the fragment size distribution for the mesh sizes 0.5 mm and 0.2 mm, roughly the size
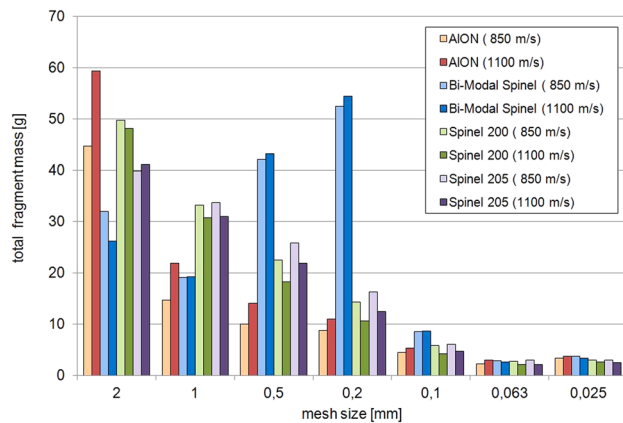
Fig. 9 Fragment mass distribution from sieve analysis; mean values from three tests with each configuration
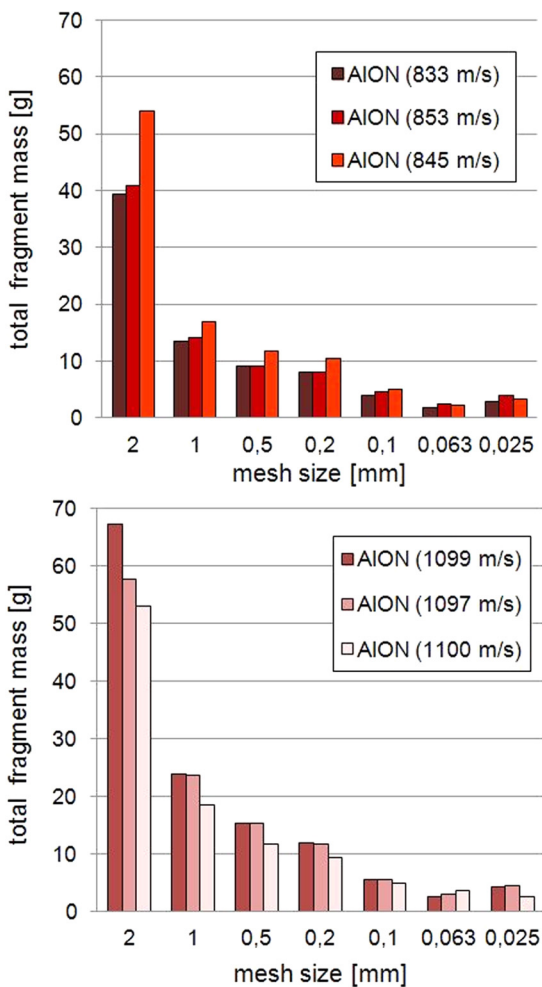

Fig. 10 Fragment mass distribution for AlON at 850 m/s (left) and 1100 m/s (right)

Fig. 11 Cumulative mass plot; mean values from three tests with each configuration

was found at the lower impact velocity. This result is plausible, since, at 850-m/s impact velocity, the residual penetration was almost zero. Thus, most of the kinetic energy of the projectile was dissipated during the interaction with the spinel. At the higher impact velocity of 1100 m/s, a considerable residual penetration occurred, combined with bulging and crack formation in the backing plate.

Fragments from the 0.2-mm size class of AlON and the bimodal spinel were analyzed by means of scanning electron microscopy (SEM). Figure 12 shows a comparison of SEM micrographs from tests at both impact velocities for AlON and the bimodal spinel. With the bimodal spinel, the fragments in this size class mainly consist of single, large grains, which means that the cracks propagated along the very weak grain boundaries without much fracturing of the grains itself. This can clearly be seen from the micrograph in Fig. 13, which shows that the "fragment" is a single-faceted crystal of spinel with an isotropic tetrakaidecahedron morphology that was separated/detached from the fine grain matrix, preserving the single crystal facets and morphology without fracturing. These single crystal grains probably grew from a solution-reprecipitation mechanism, which resulted in very weak grain boundaries at these large grains, resulting in a dramatic intergranular failure/separation. There is minimal evidence of any damage on the large separated grains. The anomalous results for the size fractions at 0.5 mm and 0.2 mm occurred because the large grains of the bimodal material were just in this size range. On the other hand, the grain boundaries for the AlON material were very strong, forcing the material to fail in a transgranular mode by cleavage, absorbing more energy in their failure. This is illustrated by the micrograph in Fig. 13, showing a single cleavage fragment and also a fragment with cleavage steps with AlON. The fragmentation behavior of the fine-grained spinels was similar to that of AlON.

5.2 Particle Tracking With Laser-Light-Sheet Technique. Since the material, which is in direct contact with the projectile or in the immediate vicinity, cannot be visualized inside the target, an experimental method was developed that allows observing the fragments ejected from the crater during penetration. The key to the observation of single particles in the dense cloud of ejecta is the laser-light-sheet illumination technique, coupled with a high-speed video camera. With this method, it is possible to determine velocity and size of the ceramic ejecta as a function of time. The light-sheet technique with the adaption of a laser represents a non-invasive method to visualize single particles in a defined measuring plane with a high time resolution rate. It allows determining speed, direction of motion, and size of single particles. Figure 14 shows a schematic of the experimental setup. The punctiform laser beam is directed into a special light-sheet optic and converted into a linear divergent beam. The light segment of about 1-mm thickness is reflected by a mirror from the top of the target

range of the large grains in the bimodal spinel. Almost 60% of the complete fragment mass was found in these two size classes. This result indicates a clear difference in the fracture mode between the bimodal spinel and the other materials.

The total mass of generated fragments was higher with all types of spinel compared to AlON at both impact velocities. This is illustrated in Fig. 11, which shows the cumulative mass versus mesh size. With all materials, the higher degree of fragmentation
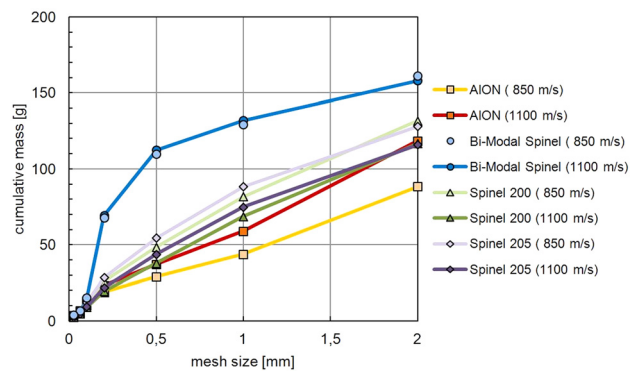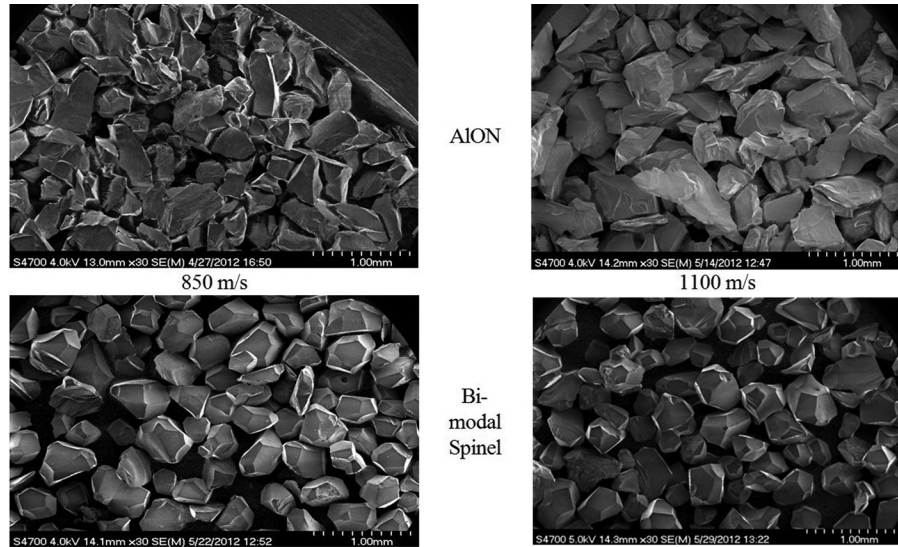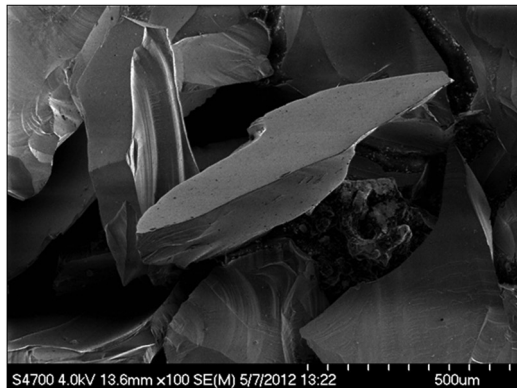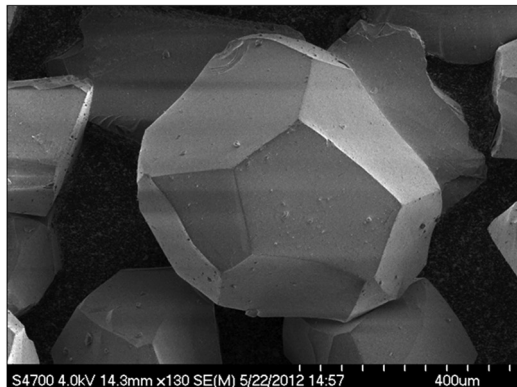
Fig. 12   Comparison of AlON and bimodal spinel fragments from 0.2-mm size class

(a)

(b)

Fig. 13   Close-up views of AlON and bimodal spinel fragments from 0.2-mm size class

Fig. 14   Schematic of the laser-light-sheet illumination technique

box in front of the ceramic. The orthogonally to the ceramic's surface-orientated light-sheet defines the measurement plane in which the particles are illuminated during the experiment. Particles outside the measurement plane are not or are only weakly illuminated. Additionally, the depth of focus of the camera, which is arranged orthogonally to the light-sheet, has to be as small as possible and exactly adjusted to the illuminated plane. This assures that only the light scattered from the fragments placed in the plane of the light-sheet is directed to the image plane. If there
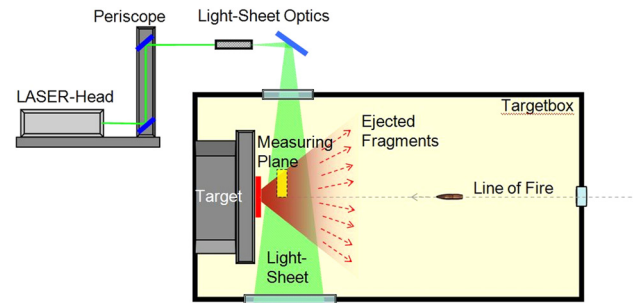
is a high density of particles, the fragments out of the measurement plane are very weakly illuminated and only appear as a fog, clearly distinguishable from the fragments staying directly in the light-sheet. Taking into consideration the possible frame rate and the image resolution of the CMOS camera, the measured area (yellow in Fig. 14) must be restricted to a small but significant array. Assuming a statistically symmetric distribution of the fragments within the cone of ejecta, the measurement plane was accomplished as an elongated rectangle above the line of fire.

Figure 15 shows the average fragment size as a function of time, determined from the tests with bimodal spinel and AlON impacted at 850 m/s and 1100 m/s, respectively. The diagram presents the fragment size distributions of the first 2 milliseconds as a moving average, which means that each data point is the mean value from the analysis of ten consecutive particles. The averaging is necessary for a useful illustration of the trend of the huge number of the calculated fragment sizes.

Due to the variation in the appearance of the first identifiable particle, the time for the first recorded data varies within a time interval of 90 μs. For both materials and impact velocities, the average fragment size was between 0.3 mm and 0.7 mm during the first 200 μs. Only with AlON at 1100 m/s, a few bigger fragments were observed in the beginning. The early phase, with identifiable particles, was followed by a period of several hundreds of microseconds duration with much less or nearly no recognized fragments. The flat part of the fragment size curve over this time period is due to the averaging process.

In the right part of the diagram (later than 1000 μs), the fragment size curves start to oscillate because of the size variation of the huge number of recognized particles. Here, the fragment size

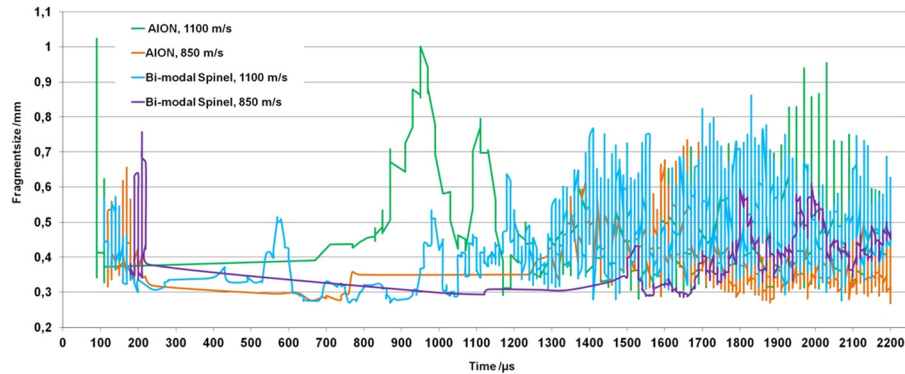**Fig. 15 Average fragment size versus time for AION and bimodal spinel (moving average, mean of ten fragments)**

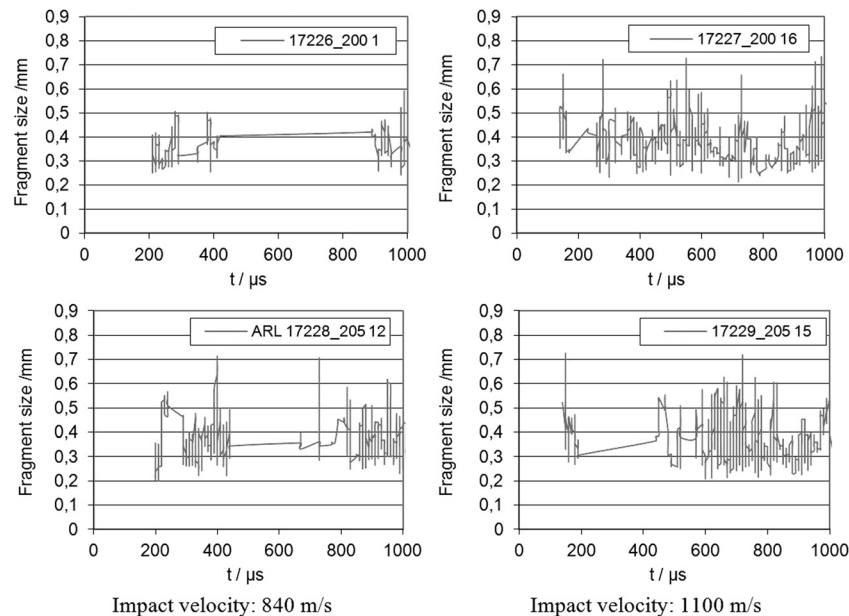Impact velocity: 840 m/s   Impact velocity: 1100 m/s

Fig. 16 Average fragment size versus time for fine-grained spinels 200 and 205 (moving average, mean of ten fragments)

is mostly in the range of 0.3 to 0.8 mm. With the bimodal spinel at 850 m/s, smaller oscillations in the fragment size curve were observed due to the lower number of fragments identified. The average fragment size did not exceed a value of 0.6 mm.

Since it is assumed that the fragments appearing initially have been in contact with the projectile and contributed to projectile erosion, the fragment sizes during the first several hundred microseconds need to be scrutinized. Figure 16 shows the first millisecond of the fragment size distributions from the tests with the fine-grained spinels. The fragment size curves of Fig. 16 also represent the moving average of ten consecutive photographs. As observed with the other materials, longer time periods occurred where no fragments could be registered.

The fact that no fragments were recognized over some time intervals does not mean that no fragments at all passed the measuring area. Fragment size below 170 μm or those which are outside the measuring plane cannot be recognized with the optical setup utilized. A further reason for the occurrence of those time intervals where no particles were recognized by the system could be an inhomogeneous spatial distribution of the fragments (see Figs. 7 and 8), so that there is a gap in the measuring plane. On the other hand, a higher density of particles can also prevent the recognition of single fragments.

In this test series, the measuring area was a rectangle of approximately 4 mm × 70 mm, positioned orthogonally above the shot axis so that theoretically all fragments ejected from the impact area at an angle $\leq$ 50 deg could be detected. With a frame rate of 100 kHz, it was possible to register particles with a velocity lower than 400 m/s. Due to the limited number of ceramic specimens available, neither a variation of the position of the measuring area within the particle cloud nor several repeated measurements were possible. This could be one reason that the clear difference in the fragmentation observed with the bimodal spinel did not appear in the in situ-measured fragment size distributions. On the other hand, different compositions of the fragment cloud during projectile penetration and the total mass of fragments collected after the test have been found with other ceramics [4]. Therefore, a further development of the method for in situ particle size measurement combined with a higher number of tests under the same conditions will be necessary in order to gain more conclusive data.

6 Conclusions

The fragmentation and ballistic resistance of three types of spinel and AlON under impact of a 7.62-mm AP projectile at 850-m/s and 1100-m/s impact velocity was analyzed. The two

fine-grained spinels and the bimodal grain-sized spinel with large grains of 250 μm diameter exhibited almost the same ballistic resistance. At 1100-m/s impact velocity, the residual penetration with AlON was significantly lower compared to the spinels.

Different methods were applied in order to study the fragmentation behavior. Sieving analysis of the recovered fragments revealed a clear difference in the fracture mode between the bimodal spinel and the other materials. Micrographs demonstrated mainly grain boundary separation/fracture in case of the bimodal spinel, whereas substantial transgranular fracture, especially along cleavage planes, occurred with AlON.

From high-speed photographs, fracture velocities were determined for all materials. Averaging the radial crack velocities at the 850- and 1100-m/s impact velocities results in the following: 0.6-μm spinel $\approx$ 2929 m/s; 1.6-μm spinel $\approx$ 3056 m/s; AlON $\approx$ 3566 m/s; and bimodal spinel $\approx$ 3722 m/s.

The size distribution of the ceramic fragments shortly after formation and ejection from the crater area was analyzed by means of the laser light-sheet illumination technique coupled with a high-speed video camera. The measurements have demonstrated the capabilities of the light-sheet technique for in situ particle detection and size measurement during the penetration process.

Acknowledgment

References

[1] Patel, P. J., Gilde, G. A., Dehmer, P. G., and McCauley, J. W., 2000, "Transparent Armor," AMPTIAC Q., **4**(3), pp. 1–6.

[2] Patel, P. J., Gilde, G. A., Dehmer, P. G., and McCauley, J. W., 2000, "Transparent Ceramics for Armor and EM Window Applications", Proc. SPIE, **4102**, p. 1.

[3] Strassburger, E., 2009, "Ballistic Testing of Transparent Armour Ceramics," J. Eur. Ceram. Soc., **29**, pp. 267–273.

[4] Strassburger, E., Hunzinger, M., and Krell. A., 2010, "Fragmentation of Ceramics Under Ballistic Impact," Proc. of 25th Int. Symposium on Ballistics, Beijing, May 17–21, pp. 1172–1179.

[5] Shockey, D. A., Bergmannshoff, D., Curran, D. R., and Simons, J. W., 2009, "Physics of Glass Failure During Rod Penetration," Ceram. Eng. Sci. Proc., **29**(6), pp. 23–32.

[6] Curran, D. R., Seaman, L., and Shockey, D. A., 1977, "Dynamic Failure in Solids," Phys. Today, **30**, p. 46.

[7] Curran, D. R., Shockey, D. A., and Simons, J. W., 2009, "Mesomechanical Constitutive Relations for Glass and Ceramic Armor," Ceram. Eng. Sci. Proc., **29**(6), pp. 3–13.

[8] Krell, A., and Strassburger, E., 2008, "Hierarchy of Key Influences on the Ballistic Strength of Opaque and Transparent Armor," Ceram. Eng. Sci. Proc., **28**(5), pp. 45–55.

[9] Krell, A., and Strassburger, E., "Discrimination of Basic Influences on the Ballistic Strength of Opaque and Transparent Ceramics," Advances in Ceramic Armor VIII, Jeffrey J. Swab, ed., Ceram. Eng. Sci. Proc., **33**(5), pp. 161–176.

[10] Schardin, H., 1950, "Results of Cinematographic Investigation of the Fracture Process in Glass," *Glastechnische Berichte* (Reports on Glass Technology), Vol. 23, Verlag der Deutschen Glastechnischen Gesellschaft, Frankfurt, pp. 325–336.

[11] Yavari, A., and Khezrzadeh, H., 2010, "Estimating Terminal Velocity of Rough Cracks in the Framework of Discrete Fractal Fracture Mechanics," Eng. Fract. Mech., **77**, pp. 1516–1526.

[12] Roberts, D. K., and Wells, A. A., 1954, "The Velocity of Brittle Fracture," Engineering, **24**, pp. 820–821.

[13] Craggs, J. W., 1960, "On the Propagation of a Crack in an Elastic-Brittle Material," J. Mech. Phys. Solids, **8**, pp. 66–75.

[14] Steverding, B., and Lehnigk, S. H., 1970, "Response of Cracks to Impact," J. Appl. Phys., **41**(5), pp. 2096–2099.

[15] Fineberg, J., Gross, S. P., Marder, M., and Swinney, H. L., 1992, "Instability in the Propagation of Fast Cracks," Phys. Rev. B, **45**, pp. 5146–5154.

[16] Senf, H., Strassburger, E., and Rothenhäusler, H., 1994, "Stress Wave-Induced Damage and Fracture in Impacted Glasses," J. Phys. IV, **4**, pp. 741–746.

[17] Ravi-Chandar, K., and Knauss, W. G., 1984, "An Experimental Investigation Into Dynamic Fracture: II. Microstructural Aspects," Int. J. Fract., **26**, pp. 65–80.

[18] Technology Assessment & Transfer, Inc., 2012, "Transparent Spinel Ceramics for Armor and Electro-Optical Applications," Spinel Data Sheet, TA&T Inc., Annapolis, MD.

[19] Goldman, L. M., Balasubramanian, S., Nagendra, N., and Smith, M., 2010, "ALON® Optical Ceramic Transparencies for Sensor and Armor Applications," www.surmet.com